

Histo-Diffusion: A Diffusion Super-Resolution Method for Digital Pathology with Comprehensive Quality Assessment

Xuan Xu^{a,*}, Saarthak Kapse^a, Prateek Prasanna^a

^aStony Brook University

ARTICLE INFO

Article history:

Received 11 Aug 2024

Keywords: Image Super Resolution, Digital Pathology, Diffusion models

ABSTRACT

Digital pathology has advanced significantly over the last decade, with Whole Slide Images (WSIs) encompassing vast amounts of data essential for accurate disease diagnosis. High-resolution WSIs are essential for precise diagnosis but technical limitations in scanning equipment and variability in slide preparation can hinder obtaining these images. Super-resolution techniques can enhance low-resolution images; while Generative Adversarial Networks (GANs) have been effective in natural image super-resolution tasks, they often struggle with histopathology due to overfitting and mode collapse. Traditional evaluation metrics fall short in assessing the complex characteristics of histopathology images, necessitating robust histology-specific evaluation methods.

We introduce Histo-Diffusion, a novel diffusion-based method specially designed for generating and evaluating super-resolution images in digital pathology. It includes a restoration module for histopathology prior and a controllable diffusion module for generating high-quality images. We have curated two histopathology datasets and proposed a comprehensive evaluation strategy which incorporates both full-reference and no-reference metrics to thoroughly assess the quality of digital pathology images.

Comparative analyses on multiple datasets with state-of-the-art methods reveal that Histo-Diffusion outperforms GANs. Our method offers a versatile solution for histopathology image super-resolution, capable of handling multi-resolution generation from varied input sizes, providing valuable support in diagnostic processes.

© 2024 Elsevier B. V. All rights reserved.

1. Introduction

In recent years, the field of digital pathology has seen a marked increase in interest, driven primarily by the increased availability of Whole Slide Images captured through advanced scanners. WSIs, known for their considerable data size, often amounting to several gigabytes per slide, contain tens of thousands of nuclei and other primitives essential for detailed analysis necessary in disease diagnosis. Consequently, high-resolution WSIs are crucial for enabling precise visualization, improving diagnostic accuracy, and facilitating automated analysis and accurate measurements.

However, the technical limitations of scanning equipment and slide preparation variability make obtaining the high-resolution images a great challenge Farahani et al. (2015); Zarella et al. (2019). The resolution of WSIs is directly tied to the capabilities of the scanning equipment and some scanners may not

have sufficiently high-resolution optics or sensors, especially the older or more budget-conscious models. Also, sometimes a compromise is made by resorting to lower resolution to keep file size manageable for image processing and transmission. Additionally, the quality of the initial slide preparation, including tissue sampling, processing and staining can greatly affect the final image resolution. Inconsistencies or deficiencies in any of above steps can lead to lower-quality images Smith et al. (2021); Dunn et al. (2024). Besides, the type and quality of staining techniques can influence the resolution and clarity of the images Runz et al. (2021). Uneven or poor staining can mask or blur important details, effectively reducing the usable resolution of the images. Therefore, it is important to find a way to synthesize the high-resolution images from low-resolution ones while keeping the finer details and subtleties of tissue and cellular structures. Super-resolution (SR) offers a promising approach to addressing this challenge. Image super-resolution encompasses a suite of image processing techniques aimed at reconstructing high-resolution (HR) images from their low-resolution (LR) counterparts.

*Corresponding author: Stony Brook University

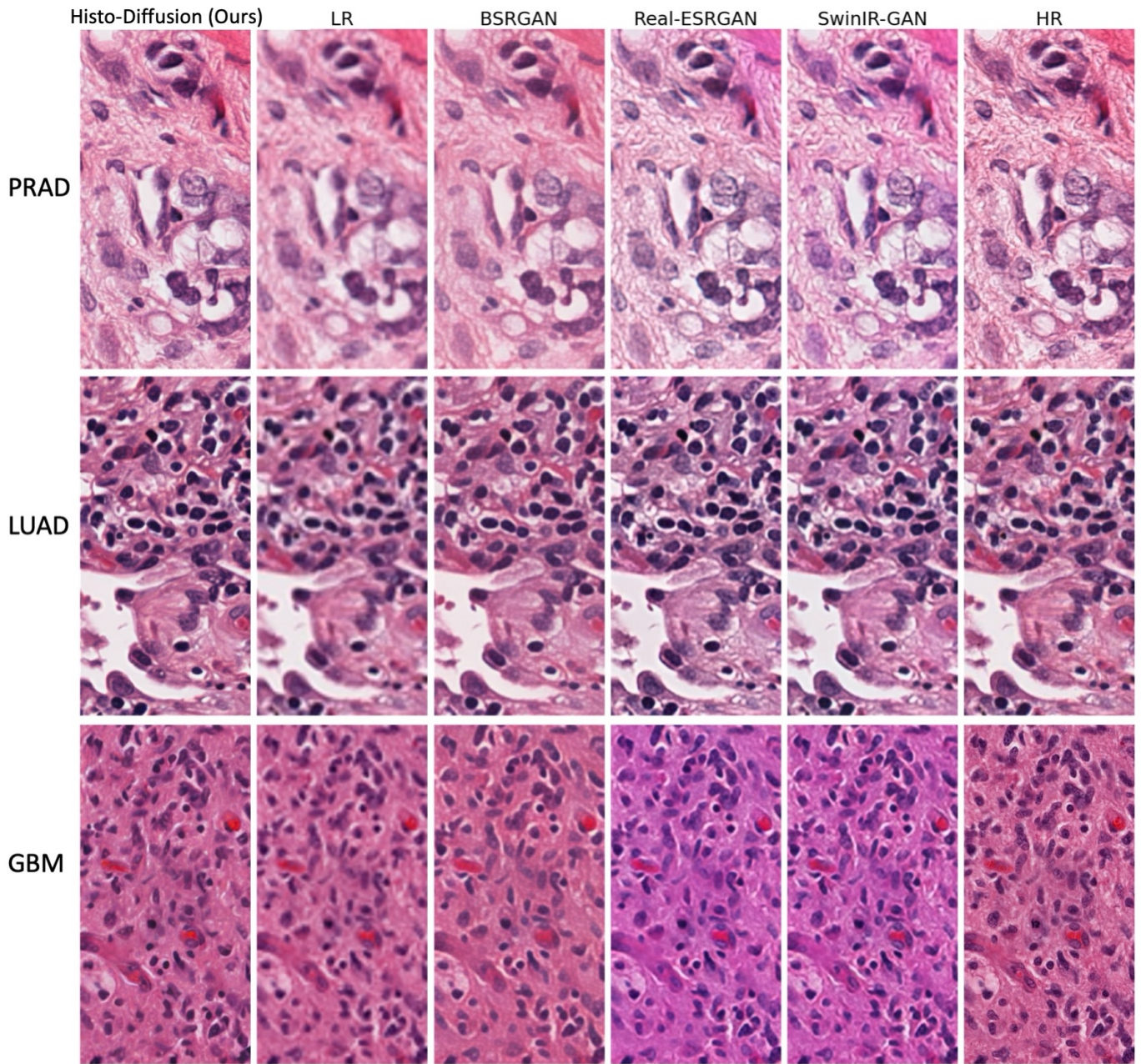


Fig. 1: Comparisons of state-of-the-art methods and Histo-Diffusion.

Deep learning has significantly propelled advancements in image super-resolution within the natural image domain. Since 2017, Generative Adversarial Networks have been increasingly applied to image super-resolution tasks Ledig *et al.* (2017a); Goodfellow *et al.* (2020); Ma *et al.* (2020); Jose *et al.* (2021); Manuel *et al.* (2022). Their proficiency in synthesizing high-fidelity images has elevated them to prominence in this domain. Specifically for natural images, GANs can generate high-resolution images with remarkable detail, accurately simulating authentic high-resolution visuals. The adversarial training approach enables GANs to iteratively refine their generative capabilities, continually improving image quality to challenge the discriminator's ability to distinguish them as synthetic.

However, training GANs often faces instability due to the ad-

versarial interactions between the generator and discriminator. Such instability may lead to mode collapse, where the generator produces only a limited variety of outputs, and non-convergence, where the models fail to reach equilibrium Thanh-Tung and Tran (2020); Saxena and Cao (2021). Consequently, GANs struggle to fully capture the diversity of histopathology images and to provide the finer details necessary for accurate diagnosis in histopathology. This presents significant challenges for realistic image synthesis and evaluation.

Diffusion models have recently gained great success in natural image synthesis tasks Dhariwal and Nichol (2021); Ho *et al.* (2020); Nichol and Dhariwal (2021). They are known for their ability to generate high-quality, realistic images. Intrinsicly, diffusion models gradually denoise an image, starting from a

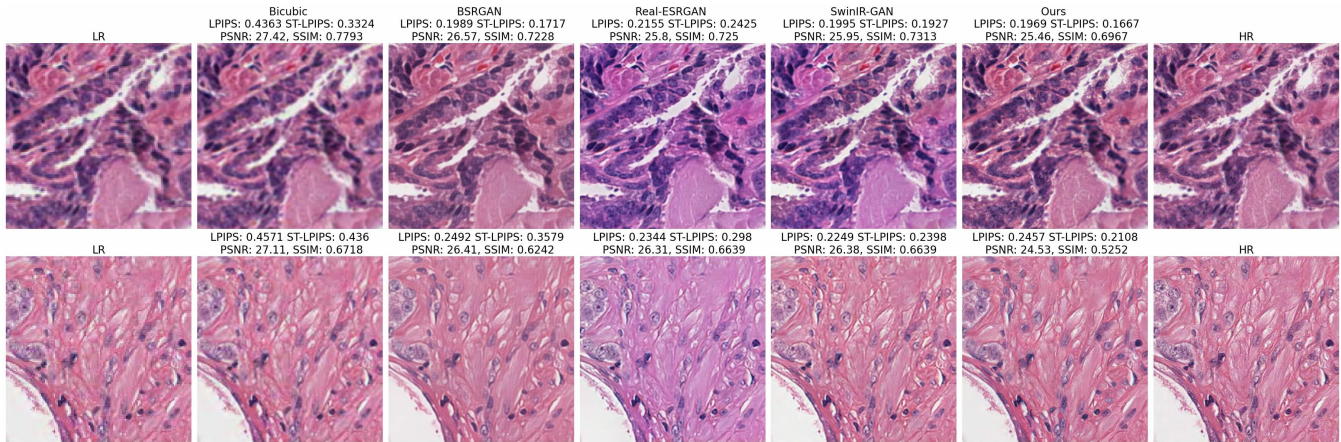


Fig. 2: Evaluation examples using PSNR, SSIM, and LPIPS in the field of digital pathology image super-resolution. Generative super-resolution methods produce images with sharper details and closer resemblance to high-resolution ground truths compared to bicubic interpolation. However, bicubic images often achieve higher PSNR, SSIM scores. Despite higher scores, bicubic images appear blurrier to human observers, indicating a disconnect between these metrics and human perception of image quality.

random noise distribution. This process makes them inherently robust to noise, rendering them particularly efficacious in the enhancement of low-resolution or qualitatively compromised imagery. Their formidable generative capacities facilitate the interpolation of absent details through the synthesis of plausible textures and patterns, even when such elements are conspicuously unclear in the low-resolution images. In the context of digital pathology, this means producing super-resolved images that maintain the integrity and authenticity of the original biological structures, which is crucial for accurate diagnosis and analysis. Pathology images often contain complex textures and patterns that are essential for disease diagnosis. Diffusion models are particularly adept at handling these complexities, ensuring that the finer details of cellular structures are accurately represented in the super-resolution images. These models are inherently robust to noise and variations in the input data, an important feature when dealing with pathology images that may have inconsistencies due to different preparation techniques or imaging conditions. The robustness of diffusion models has significantly increased their utilization in digital pathology, particularly for applications such as data augmentation, synthetic data generation, and out-of-distribution detection Pozzi *et al.* (2023); Linmans *et al.* (2024); Oh and Jeong (2023). By addressing challenges related to data scarcity and variability in histopathological images, these models enhance anomaly detection and ensure robustness in diagnostic systems through their ability to capture intricate patterns within pathology images. Although the potential of super-resolution techniques in the digital pathology field remains underexplored, the demonstrated capabilities of diffusion models suggest they can effectively capture complex structures and generate high-quality images in histopathology.

In the context of histopathology images, the accuracy and reliability of generated images are critical for downstream diagnostic and prognostic tasks. Therefore, robust evaluation metrics are essential to ensure the clinical viability of super-resolution images. Recently, tailored evaluation metrics have been pro-

posed for medical image analysis, particularly in radiology Muddeng *et al.* (2022); Maruyama (2023). However, there is a lack of metrics specifically designed for histopathology image super-resolution. As a result, research in this area often relies on natural image quality assessment (IQA) metrics to evaluate histopathology super-resolution images Afshari *et al.* (2023). Metrics like PSNR (Peak Signal-to-Noise Ratio), SSIM (Structural Similarity Index Measure), and LPIPS (Learned Perceptual Image Patch Similarity) Zhang *et al.* (2018), despite their widespread use in natural image quality assessments, can produce misleading results in histopathology, as illustrated in the caption details of Fig. 2.

Therefore, there is a pressing need for a methodology that works for histopathology image super-resolution while also providing reliable evaluation of the generated images. The super-resolution model should consider the intricate characteristics of digital pathology images and the histopathological microenvironment. Evaluation metrics should also accurately assess the similarity between generated super-resolution images and their high-resolution counterparts while effectively accommodating the variability in color, texture, and structure that results from diverse staining techniques and tissue types.

In this paper, we first introduce Histo-Diffusion to generate super-resolution images specifically for digital pathology as shown in Fig. 1. Next, we present an effective methodology for evaluating the quality of these generated images.

Our key contributions are:

- **Novel Evaluation Methodology:** We are the first to identify the sub-optimality in applying IQA metrics to the histopathology image super-resolution task. We point out the limitations of both full-reference and no-reference IQA metrics in evaluating histopathology images. These metrics fall short in assessing the complex microenvironment and structural details in histopathology images, which are crucial for accurate diagnosis. To address these issues, we propose a comprehensive evaluation methodology specif-

ically tailored for digital pathology images. This methodology incorporates both full-reference metrics (comparing the generated super-resolution images to their ground truth counterparts) and no-reference metrics (trained on our histopathology IQA dataset). It evaluates fidelity, realism, and similarity to high-resolution ground truth images. Additionally, for the first time, we employ the CLIP model Radford et al. (2021); Wang et al. (2023a) to assess image quality by measuring the alignment of generated images with human-like perception in histopathology.

- **Histopathology IQA Dataset:** We curated a histopathology image quality assessment dataset using the TCGA database, addressing the absence of available datasets for no-reference IQA metric training. Each image is assigned a quality score based on noise level, facilitating future histopathology IQA tasks and enabling accurate assessment of sharpness and noise in histopathology image super-resolution.
- **Histo-Diffusion:** We have proposed Histo-Diffusion, adapted from DiffBIR Lin et al. (2023), as the first application of diffusion models for super-resolution image generation in digital pathology. Capable of handling multiple super-resolution scales and adaptable across various cancer types, Histo-Diffusion represents a significant advancement over current state-of-the-art methods.
- **Detailed Comparative Analysis:** Our comprehensive comparative analysis highlights the effectiveness of Histo-Diffusion and provides an in-depth evaluation of diffusion versus GAN-based super-resolution methods. Across various cancer domains, Histo-Diffusion achieves the best ST-LPIPS scores, with improvements of 12.93% for PRAD, 20.83% for LUAD, and 12.88% for GBM compared to the second-best GAN-based methods. Additionally, we enhance no-reference performance with MUSIQ score improvements of 13.26% for PRAD, 16.40% for LUAD, and 3.97% for GBM. We also increase texture and intensity similarity by 17.96% (PRAD-texture), 17.19% (GBM-texture), 19.74% (PRAD-intensity), and 9.77% (GBM-intensity). This analysis provides critical insights for researchers, enabling them to identify the most suitable approach for their specific requirements.

2. Related Work

Histopathology Image Super-Resolution. Deep learning has become the predominant approach for super-resolution tasks in histopathology imaging. The specific challenges of super-resolution in this field began to receive notable attention around 2018, as evidenced by Mukherjee et al.'s use of CNNs for reconstructing high-resolution images in digital pathology Mukherjee et al. (2018). This approach was expanded with the development of a recurrent CNN model designed to generate super-resolution images from multi-resolution WSI datasets Mukherjee et al. (2019).

Concurrently, GANs were also being applied to image super-resolution tasks, with SRGAN Ledig et al. (2017b) becoming

the first framework to produce photo-realistic natural images for 4x upscaling factors using a perceptual loss function that combines adversarial and content loss. Subsequently, Enhanced SRGAN (ESRGAN) Wang et al. (2018) improved upon SRGAN by incorporating the Residual-in-Residual Dense Block (RRDB) without batch normalization. Further advancements were made with the introduction of Real-ESRGAN Wang et al. (2021), which employed a sophisticated degradation modeling process to better simulate real-world image degradation. This technique has since become a popular method for super-resolution in histopathology imaging Rong et al. (2023).

In 2020, the introduction of vision transformers significantly advanced performance in imaging tasks, leading to the creation of SwinIR Liang et al. (2021), a model specifically designed for image restoration. SwinIR has demonstrated notable success in real-world super-resolution scenarios Puttagunta et al. (2022); Zhang et al. (2022); Choi et al. (2023).

Afshari et al. (2023) conducted a comparative study in histopathology image super-resolution, using CNN-based and GAN-based models to assess the quality of super-resolved histopathology images. As depicted in Fig 3, GAN-based methods struggle to preserve stain color and intricate microenvironment details when generating super-resolution histopathology images.

Diffusion Models. Since their inception around 2020, diffusion models have become increasingly prominent across various fields of image generation and restoration, due to their ability to produce high-quality, coherent images. A pivotal development in this domain is the Denoising Diffusion Probabilistic Models (DDPMs) Ho et al. (2020). DDPM employs a Markov chain to incrementally convert noise into samples from the data distribution, substantially boosting the generative prowess of diffusion models and notably enhancing the quality of the output. The Score-Based Generative Model Song et al. (2020), innovates by utilizing stochastic differential equations to model the data distribution's gradient. This model has demonstrated its competitive edge, proving capable of generating high-quality samples across diverse applications.

SR3 Saharia et al. (2022), the first super-resolution model based on diffusion models, iteratively upgrades low-resolution images to high-resolution outputs. It excels at managing large upscaling factors, such as 8x and 16x, while maintaining high image fidelity. Cascaded diffusion models Ho et al. (2022), from the same group, consist of a series of diffusion models each designed to stepwise enhance the image resolution. This strategy allows for more controlled image refinement, thereby improving detail retention in super-resolved images.

Concurrently, the Latent Diffusion Model (LDM) Rombach et al. (2022) was proposed, quickly becoming the standard for high-resolution image synthesis. Unlike SR3 and cascaded models, LDM operates within a compressed latent space, enabling diffusion models to scale efficiently and produce high-resolution images with less computational overhead while still delivering remarkable image quality. On this foundation, the

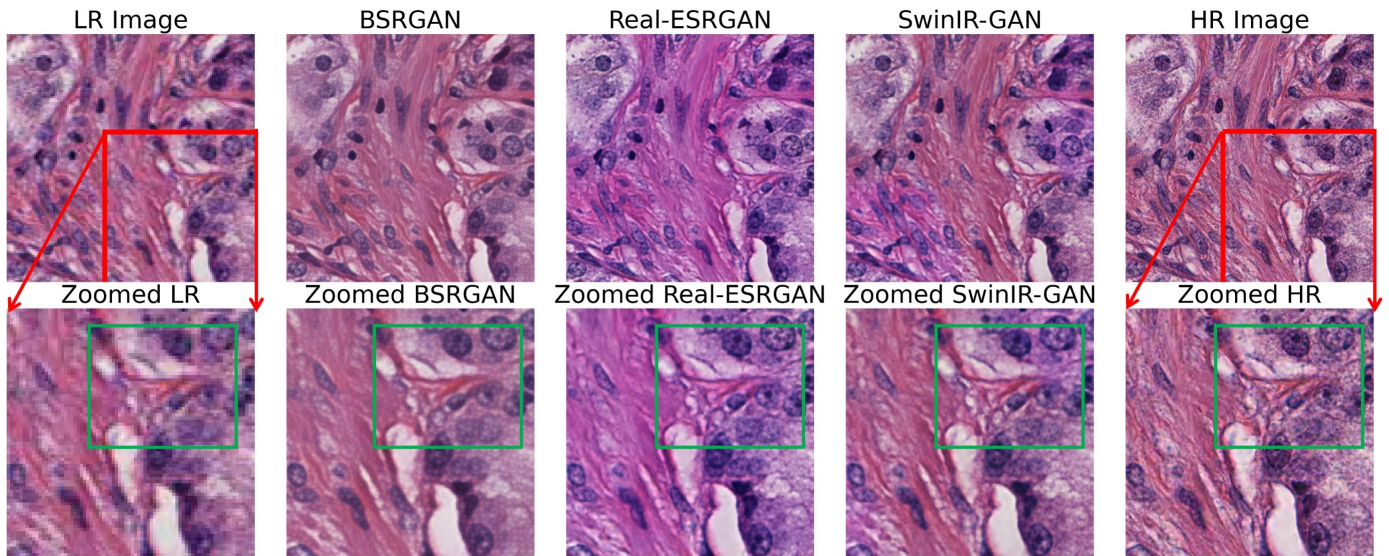


Fig. 3: Generated super-resolution images using GAN-based methods. These methods struggle to preserve stain color in histopathology images. The zoomed-in regions in the right corner of the high-resolution ground truth image, highlights that the GAN-generated super-resolution images exhibit over-smoothing and lack critical texture information within the green box, which are very crucial to accurate diagnosis.

same team Rombach et al. (2022) developed Stable Diffusion, which merges latent diffusion models with techniques from variational autoencoders (VAEs) conditioned on textual prompts. This process facilitates the creation of images that closely mirror the descriptions, establishing it as the current SOTA method for generating high-quality images from textual descriptions. This advancement has also provide a way for applying diffusion models in the field of histopathology imaging. Xu et al. (2023); Yellapragada et al. (2024); Graikos et al. (2023).

Expanding on this framework, ControlNet Zhang et al. (2023) was developed to embed additional control mechanisms beyond textual descriptions into stable diffusion. It leverages the generative diffusion prior of stable diffusion, trained on natural images, and demonstrates effective control over stable diffusion in image generation with various conditioning inputs such as canny edges, user scribbles, and human poses. This control mechanism makes ControlNet highly effective in natural image super-resolution, and a few studies Lin et al. (2023); Wang et al. (2023b) have begun incorporating low-resolution images as control inputs to generate high-resolution images. They utilize stable diffusion's powerful generative prior with an architecture similar to ControlNet. Because of its robustness against noise and its ability to produce high-fidelity super-resolution images, these approaches has found success in natural image super-resolution.

Consequently, ControlNet offers a control mechanism for the generation process in image super-resolution without the need to retrain the stable diffusion model, which demands significant time and computational resources. It enables the application of stable diffusion to super-resolution tasks. In the context of histopathology image super-resolution, the key challenge is to harness the diffusion prior and include histopathological information to generate high-resolution images that preserve essen-

tial contextual information and complex microenvironments, critical for accurate diagnosis.

Evaluation Metrics in Super-Resolution. Image quality assessment metrics are divided into two categories: full-reference IQA metrics, which compare a generated image to a high-quality reference image, and no-reference IQA metrics, which evaluate image quality without any reference.

Commonly used full-reference metrics for natural images include PSNR, SSIM, and LPIPS. PSNR measures the discrepancy between a super-resolution image and its high-resolution counterpart by calculating the peak signal-to-noise ratio. While useful for detecting overall pixel errors, PSNR is overly sensitive to noise, which is prevalent in pathological images due to staining and scanning artifacts. Simple pixel-wise comparisons fail to capture the nuanced tissue structures and cellular morphology necessary for diagnosis. SSIM examines changes in structural information, luminance, and contrast to assess image quality. Although better aligned with human perception than PSNR, SSIM might overlook crucial histopathological features like complex micro-environment and structural information, which are essential for accurate diagnosis. SSIM also struggles to evaluate images at different scales or resolutions, which is a frequent challenge in digital pathology. LPIPS Zhang et al. (2018), a recent deep-learning metric used to evaluate perceptual similarity, depends heavily on the characteristics of its training data. ShiftTolerant-LPIPS (ST-LPIPS) Ghildyal and Liu (2022), developed on the foundation of the LPIPS metric, is an enhanced perceptual similarity metric that integrates tolerance to small spatial shifts, thereby increasing its robustness and reliability for various image comparison tasks. Because these models were primarily trained on natural images, they may not fully comprehend the nuances of pathology images and could miss critical structures. Figure 2 illustrates the limitations of PSNR, SSIM, and LPIPS in digital pathology super-

resolution. Images produced via bicubic interpolation can, interestingly, score higher in these metrics despite being blurry, emphasizing the need for metrics that can accurately evaluate texture and intensity, which are crucial for clinical interpretation.

Another possible approach for evaluating generated super-resolution images is no-reference metrics. While full-reference IQA metrics evaluate the resemblance between original high-resolution images and generated super-resolution images, no-reference IQA (also known as blind IQA) assesses images without a reference. It focuses on inherent features, making it especially useful in scenarios where no ideal reference image is available. However, no-reference IQA requires datasets with image-quality score pairs for training, which are not available in histopathology.

3. Methodology

The task of image super-resolution (SR) can be formally defined as a process of generating a high resolution (HR) image from low-resolution (LR) observations of the same scene. The goal is to reconstruct a high-fidelity image that is as close as possible to the original, unseen high-resolution image, both in terms of pixel values and perceptual quality.

Given:

- An input low-resolution image I_{LR} , which is typically a downsampled version of a high-resolution image I_{HR} , possibly also degraded by factors such as blur, noise and compression artifacts.
- A desired upscaling factor s , which specifies how much larger the high-resolution image should be compared to the low-resolution input. This factor is usually expressed as a multiplier for both the width and height dimensions ($s \times width, s \times height$).

Target:

- To construct a super-resolution image I_{SR} that maximizes the fidelity to the original high-resolution source image I_{HR} , from which I_{LR} was derived.

Drawing inspiration from Lin et al. (2023), we adopt a dual-stage framework for histopathology image super-resolution task. This framework includes a restoration module to provide histopathology prior and a controllable diffusion module derived from ControlNet Zhang et al. (2023) for histopathology image generation. This dual-stage approach addresses the super-resolution challenges specific to histopathology images. The restoration module reduces the degradations and generates a histopathology-specific prior, serving as the condition for the controllable diffusion module. This controllable diffusion module ensures stable diffusion by utilizing models pretrained on natural images, while the restoration module customizes the stable diffusion specifically for histopathology applications. We also propose a comprehensive evaluation strategy to tackle the difficulties associated with applying traditional image quality assessment metrics to the histopathology imaging. Overall, our

paper offers a holistic solution for the generation and evaluation of super-resolution histopathology images.

3.1. Restoration module

To accurately replicate the complex microenvironments and artificial noise characteristics encountered in histopathology image super-resolution, we employ a restoration module utilizing the SwinIR Liang et al. (2021) model to refine the fidelity and details of these degraded images.

We simulate the degradation process on high-resolution images, I_{HR} , employing advanced degradation techniques. Histopathology image super-resolution challenges include the introduction of noise, artifacts, and the complexities of the microenvironment. Key degradation techniques such as blurring, resizing, and the introduction of noise are utilized to produce corresponding low-resolution image, I_{LR} . The SwinIR model is then applied to reduce the effects of these degradations, particularly focusing on noise and compression artifacts.

The image restoration process includes three principal stages: shallow feature extraction, deep feature extraction, and high-quality image reconstruction. We follow the modified SwinIR Lin et al. (2023) approach by first downsampling the original low-resolution input image using a pixel unshuffle operation with a scale factor of 8, followed by a convolutional layer for shallow feature extraction. For deep feature extraction, we employ Residual Swin Transformer Blocks (RSTB), each containing several Swin Transformer Layers (STL). To up-sample the deep features, nearest neighbor interpolation is performed three times, with each step followed by a convolutional layer and a leaky ReLU activation layer. This process restores the image I_{LR} to its original dimensions, resulting in the final restored image I_{RM} .

The restoration module is optimized by minimizing MSE loss as defined below:

$$I_{RM} = \text{RM}(I_{LR}), \quad \mathcal{L}_{RM} = \|I_{RM} - I_{HR}\|_2^2 \quad (1)$$

Here, I_{RM} is derived through regression learning and subsequently employed to enhance the performance of the controllable diffusion module. This restoration module not only mitigates the impact of initial image degradations but also facilitates the generation of super-resolution images that are closer in quality to the original high-resolution counterparts.

3.2. Controllable diffusion module

After obtaining the restored image I_{RM} , we use it as the conditioning input for our controllable diffusion module. Leveraging the pre-trained Stable Diffusion model, the restored image serves as the condition to generate super-resolution histopathology images, as shown in Fig. 6. Our controllable diffusion module (CDM) involves two key steps: 1) encoding the restoration module into condition latent; and 2) using this condition latent to control the generation of super-resolution histopathology images.

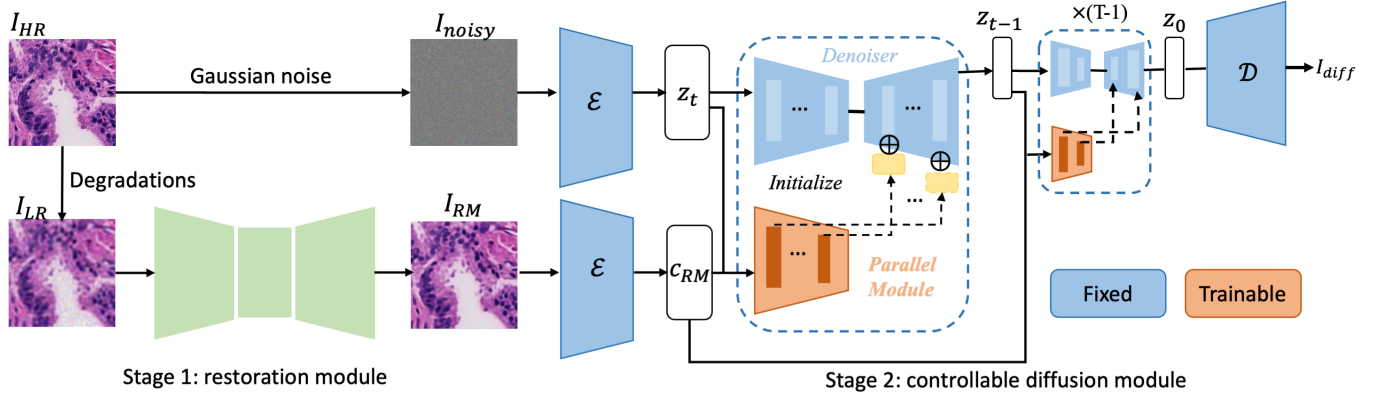


Fig. 4: Dual-Stage Diffusion-Based Image Super-Resolution Model. It includes a restoration module that generates restored images as histopathology priors for a controllable diffusion module. The restored and noisy latent images are combined to work as the input for the controllable diffusion module for super-resolution image generation.

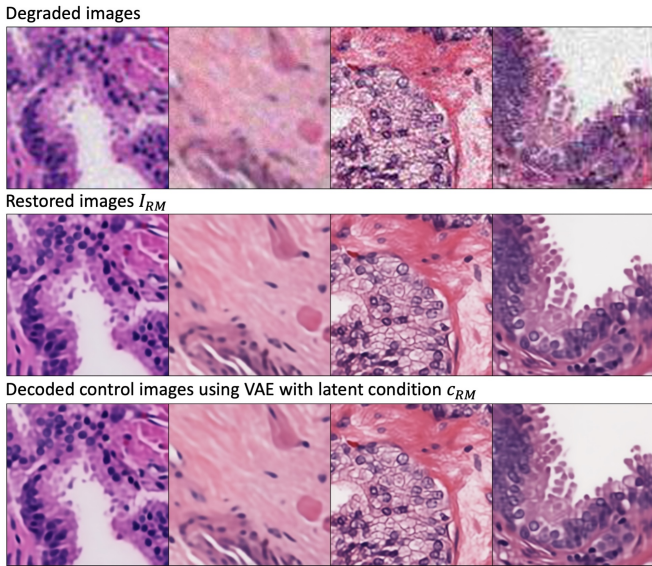


Fig. 5: Restored images with corresponding decoded control images using VAE with condition latent c_{RM}

In the first step, we take the restored image I_{RM} and leverage the VAE from Stable Diffusion to encode it into a latent space Esser et al. (2021), denoted as $c_{RM} = \mathcal{E}(I_{RM})$. As illustrated in Fig. 5, the decoded images closely resemble the restored images, demonstrating that the VAE, trained on a large-scale dataset, can accurately reconstruct the restored image I_{RM} . The conditioned latent c_{RM} captures sufficient image information from the restoration module, preserving all critical details for use in the subsequent super-resolution image generation process.

In the second step, we use the conditioned latent c_{RM} to control the Stable Diffusion generation process. Following Zhang et al. (2023); Lin et al. (2023), we make a trainable copy of the pre-trained UNet encoder and middle block, referred to as \mathbf{F}_{cond} . The conditioned latent c_{RM} is concatenated with the noisy latent z_t at time t to form the combined latent representation $z'_t = \text{cat}(z_t, c_{RM})$, where cat denotes the concatenation operation. The combined latent z'_t is fed into the control net (orange part

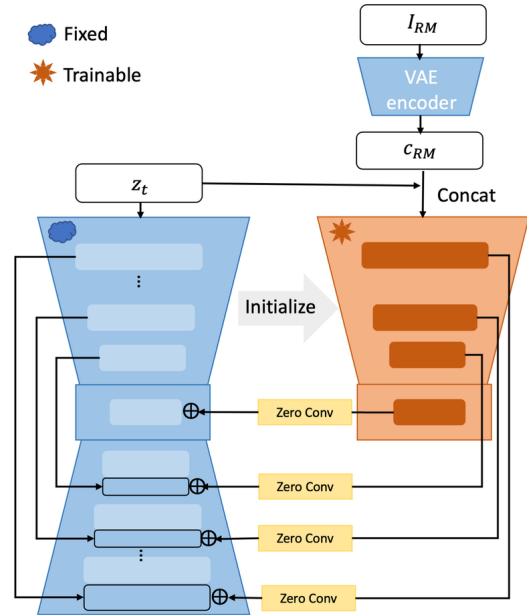


Fig. 6: Architecture of the controllable diffusion module. The right orange section represents the trainable ControlNet, while the left blue section indicates the fixed UNet. The condition latent c_{RM} is combined with noisy latent z_t to control the generation process of super-resolution images.

as shown in Fig. 6). In the default configuration of stable diffusion, the UNet in the Stable Diffusion blue region only accepted the noisy latent z_t . However, with the introduction of ControlNet in the orange region, it now accepts the combined latent z'_t as the condition. The first layer's channel number has been modified to accommodate the combined latent dimension. Feature modulation occurs solely at the middle block and through skipped connections, utilizing addition operations. Zero convolutions are strategically employed to bridge the connection between the yellow ControlNet and the fixed UNet denoiser.

During training, c_{RM} serves as the histopathology prior, and the text prompt c is set to blank (""). Only the parameters of the control net and the feature modulation are optimized by minimizing the latent diffusion objective, as shown in equation 2.

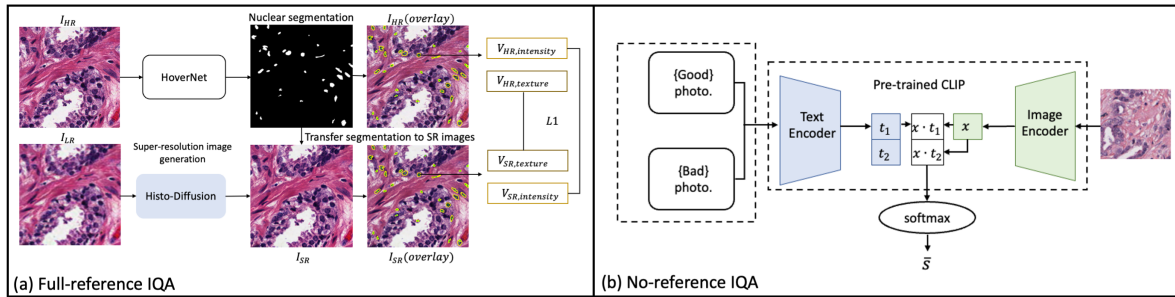


Fig. 7: Proposed IQA metric pipeline. (a) Full-reference IQA metric: High-resolution ground truth images are processed through HoverNet to obtain nuclear segmentation. Within these nuclear positions, texture and intensity information of these ground truth images are then compared to those of the generated super-resolution images. (b) No-reference IQA metric: We leverage CLIP-IQA model to assess image quality with our own curated histopathology IQA dataset.

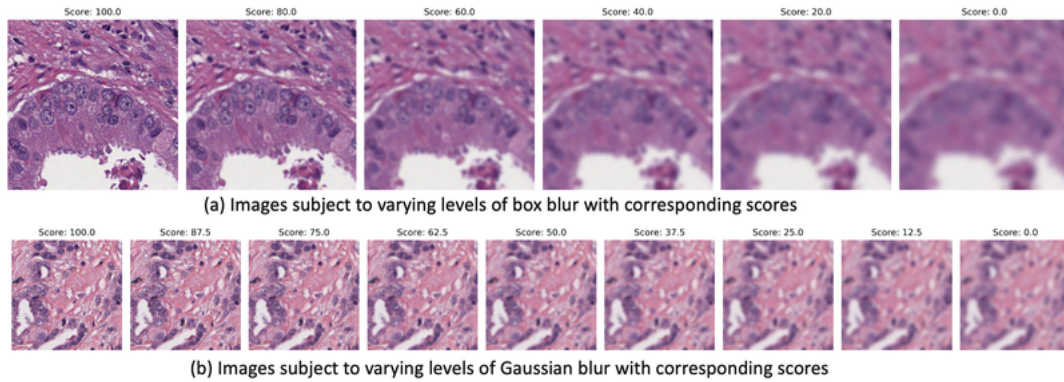


Fig. 8: Images subject to varying blur levels with corresponding Scores

This process refines the quality and resolution of the generated images based on the structured guidance provided by the concatenated latent inputs.

This targeted approach ensures that the network ϵ_θ is trained to predict the noise ϵ using c_{RM} and a blank text prompt c , effectively learning to enhance image resolution while maintaining the integrity and details necessary for accurate histopathological analysis.

$$\mathcal{L}_{CDM} = \mathbb{E}_{z_t, c, t, \epsilon, c_{RM}} [\|\epsilon - \epsilon_\theta(z_t, c, t, c_{RM})\|_2^2]. \quad (2)$$

3.3. Evaluation strategy

Current image quality assessment metrics often fall short when applied to super-resolution tasks in histopathology imaging. This is because these metrics typically rely on large natural image datasets (no-reference IQA) and fail to accurately evaluate the texture and intensity, which are crucial for clinical interpretation. In response to this deficiency, we propose a comprehensive evaluation strategy tailored specifically for digital pathology images. This strategy encompasses both full-reference and no-reference image quality assessments, designed to accurately gauge the performance of super-resolution techniques in a context where precise detail and image fidelity are paramount. This dual approach allows for a more holistic assessment of image quality, addressing both the comparison of super-resolved images to high-resolution ground truths and the intrinsic qualities of images when ground truths are unavailable.

Full-reference image quality assessment. In the realm of full-reference image quality assessment within digital pathology, our paper focuses on evaluating super-resolution images I_{SR} , against their corresponding high-resolution ground truth images, I_{HR} . Given the critical role of nuclei segmentation in the application of super-resolution techniques to histopathology images, it is imperative to determine whether I_{SR} can accurately replicate the texture and intensity characteristics of I_{HR} . For nuclei segmentation, we employed HoVer-Net Graham *et al.* (2019), a commonly utilized nuclear segmentation model, pre-trained on the CoNSeP dataset which includes 41 hematoxylin and eosin (H&E) stained image tiles, each $1,000 \times 1,000$ pixels, captured at a 40x objective magnification. The process involves inputting I_{HR} into HoverNet to identify nuclear locations, which are subsequently used to analyze corresponding areas in I_{SR} , as illustrated in Fig 7 (a).

For each generated I_{SR} , we conduct a detailed comparison of nuclei position, intensity, and texture properties against I_{HR} . For each nucleus, we calculate mean, standard deviation, skewness, and kurtosis of grayscale intensity values to form the intensity feature vector $V_{SR,intensity}$. Similarly, for texture, we measure contrast, dissimilarity, homogeneity, and energy, comprising the texture feature vector $V_{SR,texture}$. These vectors are compared to their respective ground truth vectors $V_{HR,intensity}$ and $V_{HR,texture}$ using the $L1$ metric, yielding $L1_{intensity}$ and $L1_{texture}$ differences, respectively. We employ these $L1$ values as full-reference metrics to quantify the similarity between the generated super-resolution images and the ground truth high-

resolution images.

This full-reference $L1$ metric allows us to quantitatively evaluate the fidelity of I_{SR} images in replicating critical nuclear details, assessing their similarity in texture and intensity to I_{HR} . This comparison enables us to determine which super-resolution method most accurately reflects the nuanced nuclear properties observed in high-resolution images, thus validating our super-resolution techniques both theoretically and in practical, clinical settings.

No-reference image quality assessment. Current no-reference image quality assessment (IQA) metrics are predominantly tailored for evaluating natural images by analyzing how closely an input image resembles real-world imagery. However, these metrics often fail to capture the complex textures and structures characteristic of histopathology images. To bridge this gap, we have developed a specialized histopathology image dataset with quality scores derived from the TCGA-PRAD database. We selected 5000 patches at $40\times$ magnification, representing the high-resolution ground truth with a maximum score of 10.0. For each image in this set, we introduced varying levels of noise using two types of distortion (box blur and Gaussian blur). For the box blur, the noise level was incrementally increased by adjusting the radius, with scores assigned based on the corresponding radius level. Similarly, for the Gaussian blur, the standard deviation of the Gaussian kernel was gradually increased, resulting in deteriorating scores. We curated two datasets of histopathology patches—one for box blur and the other for Gaussian blur—each rated on a scale from 10.0 (best) to 0.0 (worst, most noisy). The scores are illustrated in Fig 8.

The rationale behind selecting these specific types of noise is that generative models in histopathology image super-resolution often suffer from over-smoothing, resulting in super-resolved images that lack sharpness and detail. By employing box blur and Gaussian blur, we aim to evaluate the extent of blur and over-smoothing in generated super-resolution images. Consequently, we have created two distinct histopathology image datasets with quality scores for subsequent training of the IQA model.

To effectively learn and predict these quality scores for histopathology images, we utilize the state-of-the-art CLIP-IQA model Wang *et al.* (2023a). CLIP-IQA leverages the capabilities of the CLIP model to assess image quality through contrastive assessment and semantic alignment. As illustrated in Fig 7 (b), CLIP-IQA uses images with quality scores as inputs. Each image is processed by the CLIP model to extract feature embeddings. Similarly, textual descriptions that represent high-quality reference standards are also converted into embeddings using the CLIP model. The quality of an image is determined by comparing its embedding with those of the reference standards, which represent various quality attributes or common defects such as sharpness, color fidelity, and blurring. Higher similarity scores indicate better alignment with the reference standards, suggesting higher perceptual quality.

We trained CLIP-IQA with our specifically curated dataset, enabling it to recognize and quantify the degradation in

Table 1: Dataset distribution

	Cancer type	#Patches	#WSIs
Train	PRAD	200000	200
Val	PRAD	100	36
Test	PRAD	2000	70
	PRAD	100	70
	LUAD	100	6
	GBM	100	17

histopathology images due to blurring effects. After training, the CLIP-IQA model is employed to assess the quality of images during testing, providing a robust mechanism to evaluate image quality in a domain-specific context. The generated super-resolution images are then input into the trained CLIP-IQA to obtain quality scores CLIP-IQA (boxblur), CLIP-IQA (Gaussian), ensuring that the assessment is not only precise but also highly relevant to the specific requirements of histopathology image analysis.

4. Experiments and Results

4.1. Datasets and Evaluation Metrics

Datasets. We utilize the TCGA-PRAD dataset for curating our high-resolution (HR) and low-resolution (LR) patch-level dataset. A total of 200 WSIs were randomly selected, with an additional 70 WSIs forming our test set. No WSIs overlap between the training and test sets. The WSI ids are provided in the supplementary materials. These WSIs were tiled into smaller patches, yielding a training set of 200,000 patches and a validation set comprising 100 patches, all randomly selected from the initial 200 WSIs. For the purposes of evaluation, our dataset includes 100 TCGA-PRAD patches (PRAD-100), representing the cancer type used in training, and an expanded set of 2000 TCGA-PRAD patches (PRAD-2000) to encompass a broader testing cohort. All patches were randomly selected from 70 WSIs in TCGA-PRAD. We also incorporate 100 TCGA-LUAD (LUAD-100) patches from 6 WSIs and 100 TCGA-GBM (GBM-100) patches from 17 WSIs to assess the model’s generalization capabilities across different cancer types. For LUAD-100, each patch consists of a HR image at $40\times$ magnification (512×512 pixels) and a corresponding LR image at $10\times$ magnification (128×128 pixels). GBM-100 includes HR images at $20\times$ magnification (512×512 pixels) and LR images at $5\times$ magnification (128×128 pixels) to further test the model’s ability to handle different magnification scales. The distribution of the entire dataset is detailed in Table 1.

Implementation Details. Our framework is implemented in PyTorch and trained on Quadro RTX 8000 GPUs. We trained the restoration module for 150k iterations with a batch size of 16. For the generative prior, we employ Stable Diffusion 2.1-base and fine-tune the controllable diffusion module for 205k iterations. The AdamW optimizer is utilized Loshchilov and Hutter (2017) with a learning rate of 0.0001. For inference, we utilize spaced DDPM sampling Nichol and Dhariwal (2021) with 50 timesteps. Only the low-resolution images (128×128

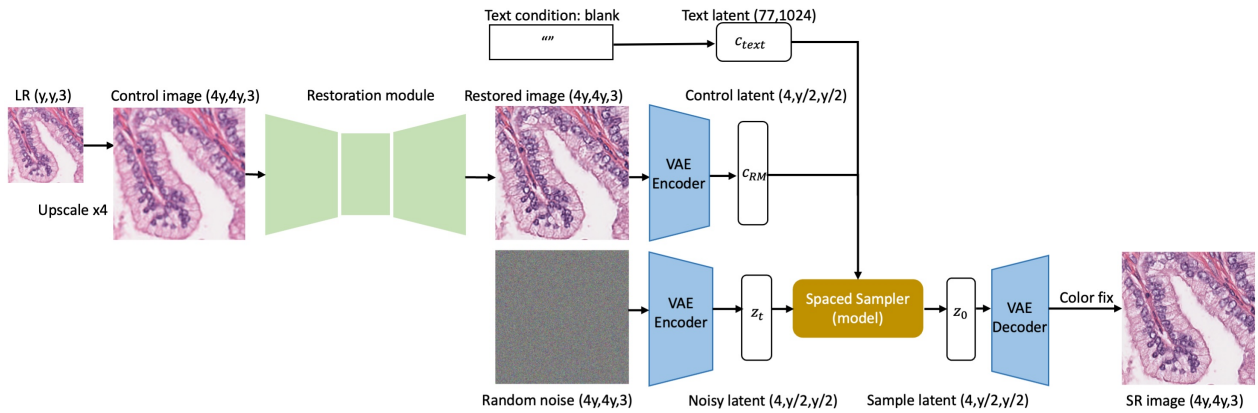


Fig. 9: Inference process of Histo-Diffusion. During inference, a low-resolution image with dimensions $(y, y, 3)$ is fed into the model for image super-resolution generation. Due to the capability of the stable diffusion’s UNet to handle any latent whose dimensions are multiples of 8, our diffusion-based super-resolution model can process any size input images. The low-resolution image is resized to the target upscaled size $(4y, 4y, 3)$ and preprocessed using the SwinIR-based restoration module to generate a restored image. This restored image is downsampled via the VAE encoder to produce the control latent. The control latent, with dimensions $(4, y/2, y/2)$, must be a multiple of 8 for the UNet in Stable diffusion, which means the control image $(4y, 4y, 3)$ must be a multiple of 64. If the control image dimensions are not multiples of 64, padding is applied to the control image to meet this requirement. Concurrently, a random noisy image with the same dimensions as the restored image is generated and encoded by the VAE to obtain the noisy latent. A blank text condition (“”) is input into CLIP to derive the text embedding. Both the control latent and text embedding are fed into the trained model with a spaced sampler to generate sample latent, which are subsequently decoded by the decoder. Color fix is then applied to these samples to finally produce the super-resolution image.

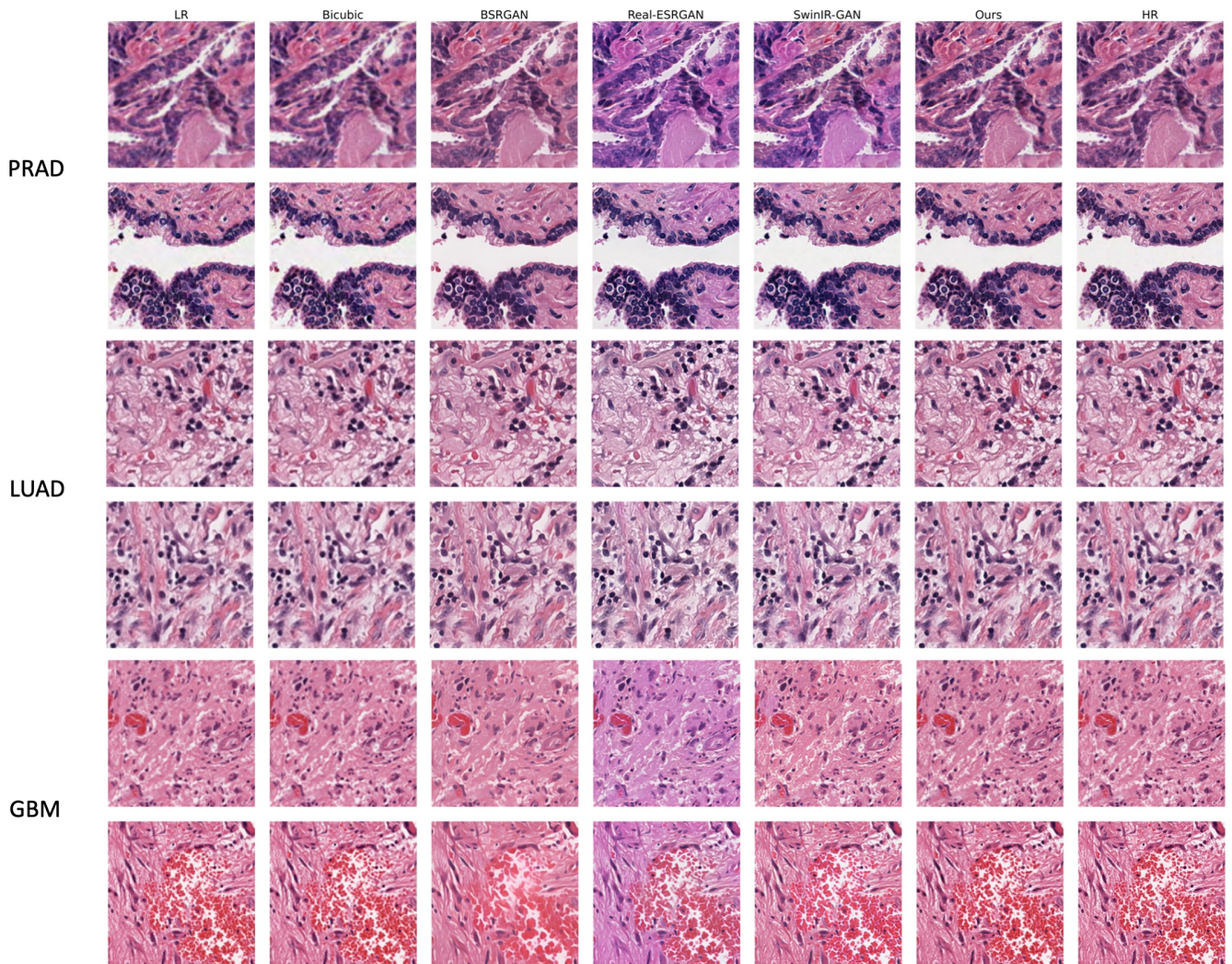


Fig. 10: Visual comparisons on PRAD-100, LUAD-100 and GBM-100 samples. Please zoom in for more details.

Table 2: Comparison with state-of-the-art GAN-based methods on histopathology image datasets with a 4× upsampling scale. The best and second best results are highlighted in **bold** and underline.

Datasets	Methods	Scale	Metrics								
			PSNR↑	SSIM↑	LPIPS↓	ST-LPIPS↓	CLIP-IQA↑	MUSIQ↑	NIQE↓	BRISQUE↓	NRQM↑
PRAD-100	Bicubic	×4	26.48	0.6656	0.4534	0.4702	0.3738	25.96	8.64	64.09	3.18
	BSRGAN	×4	<u>25.78</u>	0.6335	0.2612	0.3462	0.3851	35.93	8.57	<u>39.81</u>	4.38
	Real-ESRGAN	×4	25.49	0.6639	<u>0.2277</u>	0.2598	0.4753	<u>39.73</u>	8.82	46.71	4.61
	SwinIR-GAN	×4	25.52	0.6605	0.2229	<u>0.2388</u>	0.4499	38.87	<u>8.56</u>	44.78	<u>4.95</u>
	Ours	×4	24.86	0.5947	0.2279	0.2079	<u>0.4559</u>	45.00	4.95	31.39	6.34
LUAD-100	Bicubic	×4	28.27	0.7691	0.3462	0.3923	0.2640	30.52	7.62	56.41	3.44
	BSRGAN	×4	26.85	0.7154	0.3307	0.3085	0.3585	36.04	7.36	<u>44.29</u>	<u>3.98</u>
	Real-ESRGAN	×4	25.76	0.7311	0.3300	0.3121	0.4135	<u>37.13</u>	7.66	51.05	3.85
	SwinIR-GAN	×4	27.09	0.7577	0.3113	0.2842	0.4177	<u>35.73</u>	7.96	48.49	3.88
	Ours	×4	25.92	0.6666	0.2526	0.2250	0.4309	43.22	5.12	33.14	5.15
GBM-100	Bicubic	×4	24.34	0.5808	0.5199	0.5484	0.4540	33.44	<u>8.15</u>	52.83	3.05
	BSRGAN	×4	<u>23.39</u>	0.5199	0.3462	0.4790	0.3997	40.91	9.06	<u>38.19</u>	4.22
	Real-ESRGAN	×4	24.08	0.5846	0.3634	0.4644	0.5205	44.51	9.34	39.95	4.22
	SwinIR-GAN	×4	24.31	<u>0.6102</u>	<u>0.3436</u>	<u>0.4205</u>	<u>0.4954</u>	<u>47.25</u>	10.05	40.53	<u>4.42</u>
	Ours	×4	22.88	0.4950	0.2894	0.3663	0.4862	49.13	4.94	27.52	5.96
PRAD-2000	Bicubic	×4	27.05	0.6823	0.4398	0.4438	0.3760	26.21	8.64	62.98	3.24
	BSRGAN	×4	<u>26.26</u>	0.6479	0.2529	0.3268	0.3886	35.76	8.52	37.99	4.43
	Real-ESRGAN	×4	25.95	<u>0.6759</u>	0.2235	0.2558	0.4805	<u>39.53</u>	8.76	45.97	4.64
	SwinIR-GAN	×4	26.05	0.6740	0.2202	<u>0.2377</u>	0.4542	38.87	8.49	44.97	4.90
	Ours	×4	25.36	0.6075	<u>0.2221</u>	0.2006	<u>0.4543</u>	44.44	4.99	30.69	6.30

pixels) are input into the trained generative models to assess their performance. The inference process is illustrated in Fig 9.

Additionally, we test the capability of our Histo-Diffusion model to generate images at multiple resolutions. Due to the flexibility of Stable Diffusion’s UNet, it can handle input images of any size and perform upscaling to any desired size. This capability allows for multi-scale generation for input images of varying sizes. Patches of low-resolution (LR) images at 5×, 10×, and 20× magnifications with different image sizes are fed into the trained diffusion model, which then generates corresponding super-resolution (SR) images. This aspect of our research evaluates the model’s effectiveness in multi-resolution image generation, demonstrating its potential utility in diverse clinical scenarios.

Evaluation Metrics. We employ commonly used metrics such as PSNR (Peak Signal-to-Noise Ratio), SSIM (Structural Similarity Index Measure), LPIPS (Learned Perceptual Image Patch Similarity) Zhang et al. (2018), and ShiftTolerant-LPIPS Ghildyal and Liu (2022) to assess the fidelity of the generated super-resolution images I_{SR} in comparison to the ground truth high-resolution images I_{HR} . We also include non-reference metrics such as CLIP-IQA Wang et al. (2023a), MUSIQ Ke et al. (2021), NIQE Mittal et al. (2012b), Brisque Mittal et al. (2012a), and NRQM Ma et al. (2017) to evaluate the realism of all produced images. Additionally, beyond the commonly used metrics in natural image analysis, we apply specialized full-reference and no-reference metrics specifically designed for the histopathology image super-resolution task. Traditional full-reference metrics such as PSNR and SSIM may not adequately evaluate the complex micro-environment and structural information in histopathology images, potentially leading to misleading results, as demonstrated in Fig 2. No-reference metrics, typically trained

on natural images, lack sufficient exposure to the texture information found in histopathology images, where such details are critical for diagnosis and clinical needs. To address these limitations, we evaluate the super-resolution images using our proposed metrics. These include calculating $L1_{intensity}$ and $L1_{texture}$, as well as assessing blur levels using $CLIP-IQA(boxblur)$ and $CLIP-IQA(Gaussian)$, providing a targeted evaluation of the super-resolution images in the context of histopathology image super-resolution task.

4.2. Comparisons with State-of-the-Art Methods

We evaluate the performance of our proposed Histo-Diffusion method against various state-of-the-art methods including BSRGAN Zhang et al. (2021), Real-ESRGAN Wang et al. (2021), and SwinIR-GAN Liang et al. (2021), utilizing datasets including PRAD-100, PRAD-2000, LUAD-100, and GBM-100. We conduct a detailed examination of both quantitative and qualitative outcomes for these methods across the datasets. Our analysis includes comparisons based on image quality metrics, visual clarity, and their relevance to real-world diagnostic scenarios, providing a comprehensive evaluation of each model’s capability to enhance image resolution effectively.

Quantitative results. Low-resolution images with dimensions 128×128 are fed into various models to produce super-resolution (SR) images. As detailed in Table 2, our Histo-Diffusion model surpasses state-of-the-art models in perceptual quality, as gauged by ShiftTolerant-LPIPS Ghildyal and Liu (2022)—a recent and robust full-reference image quality assessment (IQA) metric. This metric offers a more precise evaluation than conventional metrics such as PSNR, SSIM, and LPIPS. It also yields comparable results in LPIPS, which assesses the perceptual similarity between images, indicating that our generated SR images bear a closer resemblance to high-resolution ground truth images than those produced by other

Table 3: Comparison with state-of-the-art GAN-based methods on histopathology image datasets with a 4× upsampling scale on PRAD-100, LUAD-100, GBM-100, PRAD-2000 dataset using our proposed metrics. The best and second best results are highlighted in **bold** and underline.

Datasets	Methods	Scale	Metrics			
			$L1_{texture} \downarrow$	$L1_{intensity} \downarrow$	CLIP-IQA (boxblur) \uparrow	CLIP-IQA (Gaussian) \uparrow
PRAD-100	Bicubic	×4	274.21	14.74	0.8109	0.8197
	BSRGAN	×4	348.65	20.77	0.9015	0.8776
	Real-ESRGAN	×4	321.15	15.38	0.8884	0.8974
	SwinIR-GAN	×4	321.94	15.14	0.9304	0.9288
	Ours	×4	224.95	11.83	0.9468	0.9458
LUAD-100	Bicubic	×4	160.41	11.04	0.8768	0.8943
	BSRGAN	×4	242.59	19.05	0.9010	0.8934
	Real-ESRGAN	×4	271.38	16.59	<u>0.9359</u>	<u>0.9364</u>
	SwinIR-GAN	×4	253.44	16.01	0.9307	0.9355
	Ours	×4	<u>190.49</u>	<u>13.14</u>	0.9497	0.9504
GBM-100	Bicubic	×4	<u>388.57</u>	18.00	0.7784	0.7566
	BSRGAN	×4	470.60	29.81	0.9245	0.8965
	Real-ESRGAN	×4	425.01	20.84	0.9032	0.9026
	SwinIR-GAN	×4	397.22	19.38	0.9419	0.9276
	Ours	×4	321.75	16.24	0.9513	0.9343
PRAD-2000	Bicubic	×4	257.04	14.19	0.8045	0.8177
	BSRGAN	×4	331.23	20.27	0.9029	0.8791
	Real-ESRGAN	×4	300.24	14.83	0.8908	0.8994
	SwinIR-GAN	×4	304.11	14.66	0.9308	0.9308
	Ours	×4	220.96	11.77	0.9464	0.9467

Table 4: Comparisons of with and without stage 1 restoration module. The best and worst results are highlighted in **bold** and *textit*.

Datasets	Iterations	Degradation	Metrics										Our Metrics			
			PSNR \uparrow	SSIM \uparrow	LPIPS \downarrow	ST-LPIPS \downarrow	CLIP-IQA \uparrow	MUSIQ \uparrow	NIQE \downarrow	BRISQUE \downarrow	NRQM \uparrow	$L1_{texture} \downarrow$	$L1_{intensity} \downarrow$	CLIP-IQA (boxblur) \uparrow	CLIP-IQA (Gaussian) \uparrow	
PRAD-100	160k	without stage1	25.15	0.6043	0.2368	0.2216	0.4378	43.39	4.77	29.12	6.26	241.85	12.47	0.9532	0.9540	
		with stage1	25.03	0.6081	0.2287	0.2089	0.4439	43.49	5.08	30.93	6.16	213.36	11.34	0.9541	0.9529	
LUAD-100	160k	without stage1	26.65	0.7041	0.2240	0.2213	0.4124	41.48	5.26	34.00	4.85	191.67	12.46	0.9370	0.9457	
		with stage1	26.48	0.6935	0.2576	0.2290	0.4133	41.61	5.33	33.08	4.81	176.38	12.64	0.9478	0.9519	
GBM-100	160k	without stage1	23.49	0.5292	0.2927	0.3790	0.4653	46.49	5.22	29.30	5.44	319.73	17.06	0.9566	0.9423	
		with stage1	23.25	0.5217	0.2822	0.3642	0.4767	47.39	5.05	28.36	5.85	272.71	14.06	0.9510	0.9361	

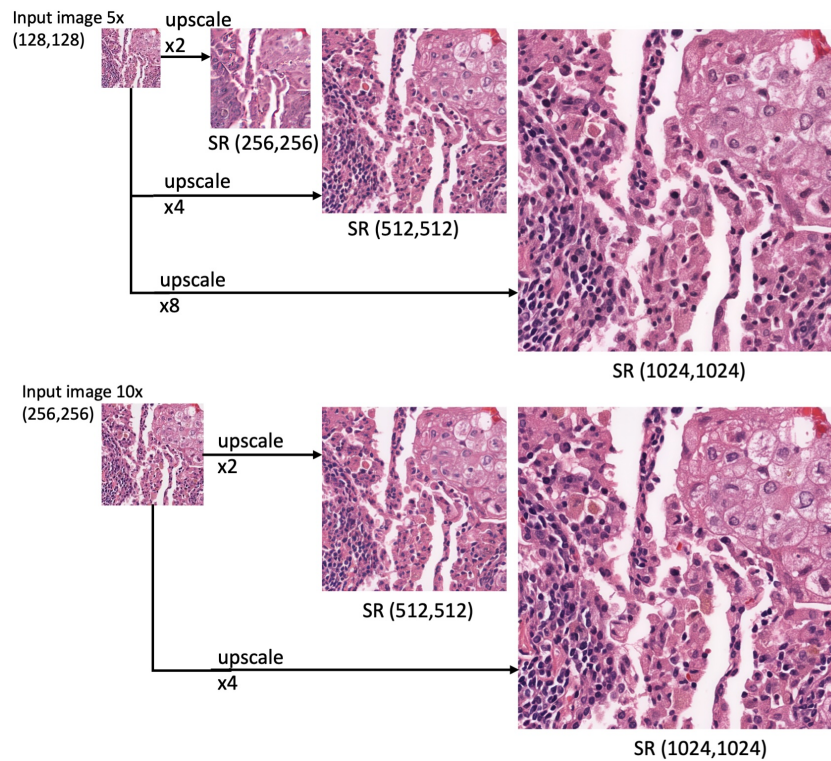


Fig. 11: Histo-Diffusion supports multi-scale super-resolution image generation, handling various input image sizes and different upsampling factors. For example, when an input image at 5x magnification with dimensions (128, 128) is provided, Histo-Diffusion can upscale it by factors of 2x, 4x, and 8x. It can also accommodate different input image sizes, as shown in the second row, where an input image at 10x magnification with dimensions (256, 256) undergoes similar upsampling. This flexibility makes Histo-Diffusion highly adaptable for diverse super-resolution tasks in digital pathology.

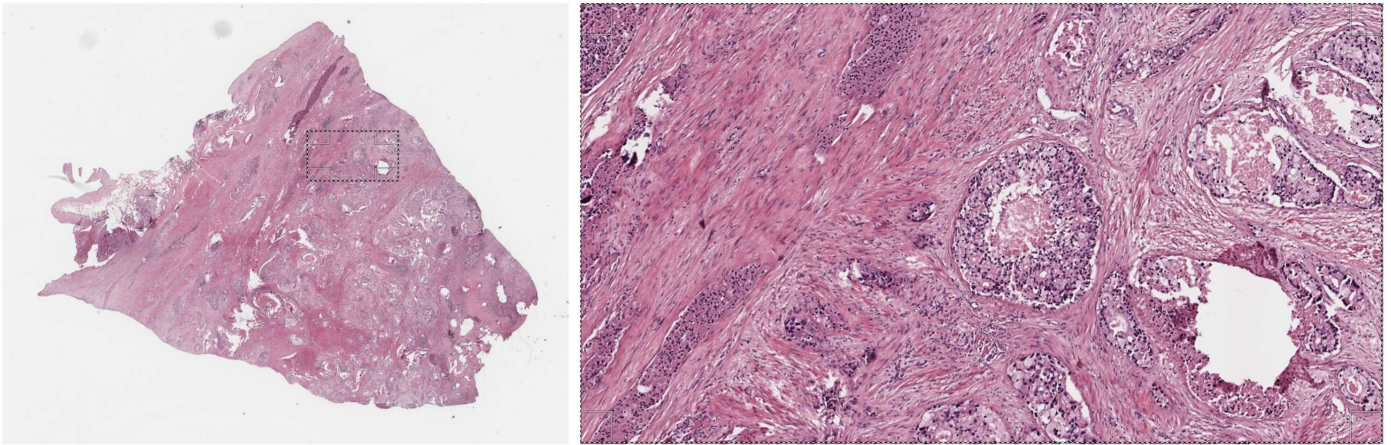


Fig. 12: A super-resolution image generated at the whole slide level. We input low-resolution images at 5x magnification into our model, which then upscales them by $\times 8$ to generate super-resolution patches. The image on the left shows the super-resolution WSI. We've zoomed into a small area within the rectangular box to highlight finer details, as shown in the image on the right. For more examples and WSI-level super resolution images, please visit more wsi level examples.

methods. In terms of no-reference metrics, our model excels in the evaluations of MUSIQ, NIQE, Brisque, and NRQM, suggesting that our generated images not only appear higher in quality but also more realistic compared to those generated by GAN-based methods. These outcomes affirm that the Histo-Diffusion model is adept at generating histopathology images with enhanced realism, outperforming existing SOTA models, particularly those utilizing GANs.

Furthermore, we assess these generated super-resolution images using our proposed full-reference and no-reference metrics, with results shown in Table 3. These results show that our method achieves the closest similarity to high-resolution ground truth images in terms of intensity and texture, highlighting that our approach can closely mimic the texture and intensity levels of the ground truth images. These characteristics, particularly the nuclei position, texture, and intensity properties, are vital for clinical and diagnostic purposes. It is crucial that these generated super-resolution images exhibit properties similar to high-resolution ground truth images in actual nuclear positions.

Additionally, our generated super-resolution images exhibit sharper details and less blurriness as depicted in Fig 10. Additional examples of generated super-resolution images can be found in the supplementary materials. Our images also display more accurate color textures compared to GAN-based methods, which sometimes produce inconsistent stain normalization colors in the generated images because they tend to overfit to the specific distribution of training data, whereas diffusion models inherently incorporate noise and iterative refinement, making them more robust to variations in stain and other inconsistencies. Moreover, our images show finer details that align closely with those in the ground truth images, demonstrating that our methods can preserve more details, learn structural information, and produce clearer details, making these images appear more realistic compared to other SOTA methods.

Multiple Upscale Super-Resolution Image Generation with Histo-Diffusion. We present multiple upscaled super-

resolution images in Figure 11. Our model is capable of handling various input image sizes and different upscaling factors. The generated super-resolution images retain texture and intensity fidelity across various input image sizes and scaling factors. This flexibility enables the use of a single trained model for multi-resolution SR image generation tasks in histopathology, significantly reducing training time and enhancing efficiency. This capability paves the way for clinical utilization, especially in scenarios where high-resolution images at 40x are scarce.

Whole Slide Image Level Super-Resolution. The Histo-Diffusion model's adaptability allows for the generation of super-resolution WSIs from lower magnification WSIs. As depicted in Figure 12, the model has effectively produced a super-resolution WSI-level image from low-resolution images at 5x. This feature is particularly advantageous for researchers who do not have access to high-resolution scanning equipment. By upgrading low-magnification images to higher resolutions, Histo-Diffusion can not only support the diagnostic process but also enhances the performance of various downstream tasks that require higher image quality. This capability ensures that detailed cellular and tissue structures are preserved and enhanced, facilitating more accurate analyses and interpretations in medical research and clinical settings.

4.3. Ablation study

We also evaluate the effectiveness of the restoration module, with results shown in Table 4. Without the stage 1 restoration module, the resized control image is directly fed into the controllable diffusion module. The results indicate that including stage 1 yields better performance in PRAD-100 and GBM-100, specifically in texture and intensity similarity compared to high-resolution ground truth images. Additionally, the CLIP-IQA scores for these two datasets are comparable. For LUAD-100, our method demonstrates improved texture similarity, CLIP-IQA scores, and comparable intensity similarity results. This suggests that the restoration module enhances im-

Table 5: Embedding Similarities for PRAD-100 dataset

	Bicubic	BSRGAN	Real-ESRGAN	SwinIR-GAN	Ours
UNI Embedding Similarity	0.7139	0.6885	0.7317	0.7818	0.8348
PLIP Embedding Similarity	0.9058	0.9394	0.9383	0.9457	0.9662

age quality and generates more realistic super-resolution images that closely match high-resolution ground truth images. Further results from the ablation study are provided in the supplementary materials.

4.4. Downstream tasks

To further assess the differences between the generated super-resolution images and ground truth high-resolution images to see whether these SR images can be leveraged for downstream tasks, we evaluate the similarity between SR embeddings and HR embeddings. For PRAD-100, we extract the UNI Chen *et al.* (2024) and PLIP Huang *et al.* (2023) embeddings for the SR images and the corresponding HR images. Then we calculate the cosine similarity between the SR embeddings and HR embeddings to measure the **Embedding Similarity**. The results have been shown in Table 5. We can see that our generated SR images’ embeddings show highest similarity scores across different foundation models, which suggests that using our generated SR images can yield similar embeddings to those of HR images. This similarity demonstrates the potential of using our generated images for further downstream tasks such as classification and segmentation.

5. Conclusions

Histo-Diffusion effectively addresses the limitations of traditional super-resolution techniques in computational pathology. Our comprehensive evaluation methodology, supported by two specially curated histopathology image quality assessment datasets, ensures a thorough quality assessment using both full-reference and no-reference metrics.

One of the key strengths of Histo-Diffusion is its ability to outperform GAN-based models, offering a versatile and adaptable solution capable of handling multi-resolution generation across varied input sizes. This approach overcomes the constraints of conventional state-of-the-art methods, which are typically limited to fixed upscale factors. Consequently, Histo-Diffusion provides a versatile solution for histopathology image super-resolution task.

The proposed evaluation metrics demonstrate that the generated super-resolution images closely align with high-resolution ground truths. This alignment makes the images well-suited for critical downstream tasks, such as nuclear segmentation and diagnostic support. This capability makes it a valuable tool when the high resolution images are not available.

Despite its advantages, Histo-Diffusion has certain limitations. Currently, our model is trained on a single cancer type (TCGA-PRAD). Despite our single cancer-type trained model showing promising performance across multiple cancer types, we believe that training on more cancer types in the future and devel-

oping a foundational super-resolution model could better capture the diversity of pan-cancer. Additionally, while our evaluation metrics are comprehensive, further validation on larger and more diverse datasets would be beneficial to fully establish the model’s robustness and reliability.

To address the current limitations, future work will focus on expanding the training dataset to include patches from all TCGA cancer types. This expansion aims to develop a foundation model for histopathology images, enhancing the diversity and applicability of Histo-Diffusion across a broader range of clinical scenarios. Additionally, we plan to further refine our evaluation metrics and explore more advanced no-reference quality assessment techniques Yang *et al.* (2022); Saha *et al.* (2023) to better capture the nuances of histopathology images.

In summary, Histo-Diffusion represents a major breakthrough in digital pathology, offering a robust, efficient, and adaptable solution for super-resolution image generation and evaluation. Its capability to produce high-quality images suitable for clinical use, combined with its comprehensive evaluation methodology, showcases its potential to become an essential tool in the computational pathology workflow.

6. Acknowledgements

Reported research was supported by the OVPR seed grant and ProFund grant at Stony Brook University, NIH 1R01CA297843-01, and NIH 1R21CA258493-01A1. The content is solely the responsibility of the authors and does not necessarily represent the official views of the National Institutes of Health.

7. Declaration of generative AI and AI-assisted technologies in the writing process

During the preparation of this work the authors used ChatGPT to correct grammatical errors. The authors reviewed and edited the content as needed and take full responsibility for the content of the publication.

References

- Afshari, M., Yasir, S., Keeney, G.L., Jimenez, R.E., Garcia, J.J., Tizhoosh, H.R., 2023. Single patch super-resolution of histopathology whole slide images: a comparative study. *Journal of Medical Imaging* 10, 017501–017501.
- Chen, R.J., Ding, T., Lu, M.Y., Williamson, D.F., Jaume, G., Song, A.H., Chen, B., Zhang, A., Shao, D., Shaban, M., et al., 2024. Towards a general-purpose foundation model for computational pathology. *Nature Medicine* 30, 850–862.
- Choi, H., Lee, J., Yang, J., 2023. N-gram in swin transformers for efficient lightweight image super-resolution, in: *Proceedings of the IEEE/CVF conference on computer vision and pattern recognition*, pp. 2071–2081.
- Dhariwal, P., Nichol, A., 2021. Diffusion models beat gans on image synthesis. *Advances in neural information processing systems* 34, 8780–8794.
- Dunn, C., Brett, D., Cockroft, M., Keating, E., Revie, C., Treanor, D., 2024. Quantitative assessment of h&e staining for pathology: development and clinical evaluation of a novel system. *Diagnostic Pathology* 19, 42.
- Esser, P., Rombach, R., Ommer, B., 2021. Taming transformers for high-resolution image synthesis, in: *Proceedings of the IEEE/CVF conference on computer vision and pattern recognition*, pp. 12873–12883.
- Farahani, N., Parwani, A.V., Pantanowitz, L., 2015. Whole slide imaging in pathology: advantages, limitations, and emerging perspectives. *Pathology and Laboratory Medicine International* , 23–33.
- Ghildyal, A., Liu, F., 2022. Shift-tolerant perceptual similarity metric, in: *European Conference on Computer Vision*, Springer. pp. 91–107.
- Goodfellow, I., Pouget-Abadie, J., Mirza, M., Xu, B., Warde-Farley, D., Ozair, S., Courville, A., Bengio, Y., 2020. Generative adversarial networks. *Communications of the ACM* 63, 139–144.
- Graham, S., Vu, Q.D., Raza, S.E.A., Azam, A., Tsang, Y.W., Kwak, J.T., Rajpoot, N., 2019. Hover-net: Simultaneous segmentation and classification of nuclei in multi-tissue histology images. *Medical image analysis* 58, 101563.
- Graikos, A., Yellapragada, S., Le, M.Q., Kapse, S., Prasanna, P., Saltz, J., Samaras, D., 2023. Learned representation-guided diffusion models for large-image generation. *arXiv preprint arXiv:2312.07330* .
- Ho, J., Jain, A., Abbeel, P., 2020. Denoising diffusion probabilistic models. *Advances in neural information processing systems* 33, 6840–6851.
- Ho, J., Saharia, C., Chan, W., Fleet, D.J., Norouzi, M., Salimans, T., 2022. Cascaded diffusion models for high fidelity image generation. *Journal of Machine Learning Research* 23, 1–33.
- Huang, Z., Bianchi, F., Yuksekogonul, M., Montine, T.J., Zou, J., 2023. A visual–language foundation model for pathology image analysis using medical twitter. *Nature medicine* 29, 2307–2316.
- Jose, L., Liu, S., Russo, C., Nadort, A., Di Ieva, A., 2021. Generative adversarial networks in digital pathology and histopathological image processing: A review. *Journal of Pathology Informatics* 12, 43.
- Ke, J., Wang, Q., Wang, Y., Milanfar, P., Yang, F., 2021. Musiq: Multi-scale image quality transformer, in: *Proceedings of the IEEE/CVF international conference on computer vision*, pp. 5148–5157.
- Ledig, C., Theis, L., Huszár, F., Caballero, J., Cunningham, A., Acosta, A., Aitken, A., Tejani, A., Totz, J., Wang, Z., et al., 2017a. Photo-realistic single image super-resolution using a generative adversarial network, in: *Proceedings of the IEEE conference on computer vision and pattern recognition*, pp. 4681–4690.
- Ledig, C., Theis, L., Huszár, F., Caballero, J., Cunningham, A., Acosta, A., Aitken, A., Tejani, A., Totz, J., Wang, Z., et al., 2017b. Photo-realistic single image super-resolution using a generative adversarial network, in: *Proceedings of the IEEE conference on computer vision and pattern recognition*, pp. 4681–4690.
- Liang, J., Cao, J., Sun, G., Zhang, K., Van Gool, L., Timofte, R., 2021. Swinir: Image restoration using swin transformer, in: *Proceedings of the IEEE/CVF international conference on computer vision*, pp. 1833–1844.
- Lin, X., He, J., Chen, Z., Lyu, Z., Fei, B., Dai, B., Ouyang, W., Qiao, Y., Dong, C., 2023. Diffbir: Towards blind image restoration with generative diffusion prior. *arXiv preprint arXiv:2308.15070* .
- Linmans, J., Raya, G., van der Laak, J., Litjens, G., 2024. Diffusion models for out-of-distribution detection in digital pathology. *Medical Image Analysis* 93, 103088.
- Loshchilov, I., Hutter, F., 2017. Decoupled weight decay regularization. *arXiv preprint arXiv:1711.05101* .
- Ma, C., Yang, C.Y., Yang, X., Yang, M.H., 2017. Learning a no-reference quality metric for single-image super-resolution. *Computer Vision and Image Understanding* 158, 1–16.
- Ma, J., Yu, J., Liu, S., Chen, L., Li, X., Feng, J., Chen, Z., Zeng, S., Liu, X., Cheng, S., 2020. PathsrGAN: multi-supervised super-resolution for cytopathological images using generative adversarial network. *IEEE transactions on medical imaging* 39, 2920–2930.
- Manuel, C., Zehnder, P., Kaya, S., Sullivan, R., Hu, F., 2022. Impact of color augmentation and tissue type in deep learning for hematoxylin and eosin image super resolution. *Journal of Pathology Informatics* 13, 100148.
- Maruyama, S., 2023. Properties of the ssim metric in medical image assessment: correspondence between measurements and the spatial frequency spectrum. *Physical and Engineering Sciences in Medicine* 46, 1131–1141.
- Mittal, A., Moorthy, A.K., Bovik, A.C., 2012a. No-reference image quality assessment in the spatial domain. *IEEE Transactions on image processing* 21, 4695–4708.
- Mittal, A., Soundararajan, R., Bovik, A.C., 2012b. Making a “completely blind” image quality analyzer. *IEEE Signal processing letters* 20, 209–212.
- Mudeng, V., Kim, M., Choe, S.w., 2022. Prospects of structural similarity index for medical image analysis. *Applied Sciences* 12, 3754.
- Mukherjee, L., Bui, H.D., Keikhosravi, A., Loeffler, A., Eliceiri, K.W., 2019. Super-resolution recurrent convolutional neural networks for learning with multi-resolution whole slide images. *Journal of biomedical optics* 24, 126003–126003.
- Mukherjee, L., Keikhosravi, A., Bui, D., Eliceiri, K.W., 2018. Convolutional neural networks for whole slide image superresolution. *Biomedical optics express* 9, 5368–5386.
- Nichol, A.Q., Dhariwal, P., 2021. Improved denoising diffusion probabilistic models, in: *International Conference on Machine Learning*, PMLR. pp. 8162–8171.
- Oh, H.J., Jeong, W.K., 2023. Diffmix: Diffusion model-based data synthesis for nuclei segmentation and classification in imbalanced pathology image datasets, in: *International Conference on Medical Image Computing and Computer-Assisted Intervention*, Springer. pp. 337–345.
- Pozzi, M., Noei, S., Robbi, E., Cima, L., Moroni, M., Munari, E., Torresani, E., Jurman, G., 2023. Generating synthetic data in digital pathology through diffusion models: a multifaceted approach to evaluation. *medRxiv* , 2023–11.
- Puttagunta, M., Subban, R., et al., 2022. Swinir transformer applied for medical image super-resolution. *Procedia Computer Science* 204, 907–913.
- Radford, A., Kim, J.W., Hallacy, C., Ramesh, A., Goh, G., Agarwal, S., Sastry, G., Askell, A., Mishkin, P., Clark, J., et al., 2021. Learning transferable visual models from natural language supervision, in: *International conference on machine learning*, PMLR. pp. 8748–8763.
- Rombach, R., Blattmann, A., Lorenz, D., Esser, P., Ommer, B., 2022. High-resolution image synthesis with latent diffusion models, in: *Proceedings of the IEEE/CVF conference on computer vision and pattern recognition*, pp. 10684–10695.
- Rong, R., Wang, S., Zhang, X., Wen, Z., Cheng, X., Jia, L., Yang, D.M., Xie, Y., Zhan, X., Xiao, G., 2023. Enhanced pathology image quality with restore-generative adversarial network. *The American Journal of Pathology* 193, 404–416.
- Runz, M., Rusche, D., Schmidt, S., Weihrauch, M.R., Hesser, J., Weis, C.A., 2021. Normalization of he-stained histological images using cycle consistent generative adversarial networks. *Diagnostic Pathology* 16, 1–10.
- Saha, A., Mishra, S., Bovik, A.C., 2023. Re-iqa: Unsupervised learning for image quality assessment in the wild, in: *Proceedings of the IEEE/CVF conference on computer vision and pattern recognition*, pp. 5846–5855.
- Saharia, C., Ho, J., Chan, W., Salimans, T., Fleet, D.J., Norouzi, M., 2022. Image super-resolution via iterative refinement. *IEEE transactions on pattern analysis and machine intelligence* 45, 4713–4726.
- Saxena, D., Cao, J., 2021. Generative adversarial networks (gans) challenges, solutions, and future directions. *ACM Computing Surveys (CSUR)* 54, 1–42.
- Smith, B., Hermsen, M., Lesser, E., Ravichandrar, D., Kremers, W., 2021. Developing image analysis pipelines of whole-slide images: Pre-and post-processing. *Journal of Clinical and Translational Science* 5, e38.
- Song, Y., Sohl-Dickstein, J., Kingma, D.P., Kumar, A., Ermon, S., Poole, B., 2020. Score-based generative modeling through stochastic differential equations. *arXiv preprint arXiv:2011.13456* .
- Thanh-Tung, H., Tran, T., 2020. Catastrophic forgetting and mode collapse in gans, in: *2020 international joint conference on neural networks (ijcnn)*, IEEE. pp. 1–10.
- Wang, J., Chan, K.C., Loy, C.C., 2023a. Exploring clip for assessing the look and feel of images, in: *Proceedings of the AAAI Conference on Artificial Intelligence*, pp. 2555–2563.

- Wang, J., Yue, Z., Zhou, S., Chan, K.C., Loy, C.C., 2023b. Exploiting diffusion prior for real-world image super-resolution. arXiv preprint arXiv:2305.07015 .
- Wang, X., Xie, L., Dong, C., Shan, Y., 2021. Real-esrgan: Training real-world blind super-resolution with pure synthetic data, in: Proceedings of the IEEE/CVF international conference on computer vision, pp. 1905–1914.
- Wang, X., Yu, K., Wu, S., Gu, J., Liu, Y., Dong, C., Qiao, Y., Change Loy, C., 2018. Esrgan: Enhanced super-resolution generative adversarial networks, in: Proceedings of the European conference on computer vision (ECCV) workshops, pp. 0–0.
- Xu, X., Kapse, S., Gupta, R., Prasanna, P., 2023. Vit-dae: Transformer-driven diffusion autoencoder for histopathology image analysis, in: International Conference on Medical Image Computing and Computer-Assisted Intervention, Springer. pp. 66–76.
- Yang, S., Wu, T., Shi, S., Lao, S., Gong, Y., Cao, M., Wang, J., Yang, Y., 2022. Maniq: Multi-dimension attention network for no-reference image quality assessment, in: Proceedings of the IEEE/CVF Conference on Computer Vision and Pattern Recognition, pp. 1191–1200.
- Yellapragada, S., Graikos, A., Prasanna, P., Kurc, T., Saltz, J., Samaras, D., 2024. Pathldm: Text conditioned latent diffusion model for histopathology, in: Proceedings of the IEEE/CVF Winter Conference on Applications of Computer Vision, pp. 5182–5191.
- Zarella, M.D., Bowman, D., Aeffner, F., Farahani, N., Xthona, A., Absar, S.F., Parwani, A., Bui, M., Hartman, D.J., 2019. A practical guide to whole slide imaging: a white paper from the digital pathology association. Archives of pathology & laboratory medicine 143, 222–234.
- Zhang, D., Huang, F., Liu, S., Wang, X., Jin, Z., 2022. Swinfir: Revisiting the swinir with fast fourier convolution and improved training for image super-resolution. arXiv preprint arXiv:2208.11247 .
- Zhang, K., Liang, J., Van Gool, L., Timofte, R., 2021. Designing a practical degradation model for deep blind image super-resolution, in: Proceedings of the IEEE/CVF International Conference on Computer Vision, pp. 4791–4800.
- Zhang, L., Rao, A., Agrawala, M., 2023. Adding conditional control to text-to-image diffusion models, in: Proceedings of the IEEE/CVF International Conference on Computer Vision, pp. 3836–3847.
- Zhang, R., Isola, P., Efros, A.A., Shechtman, E., Wang, O., 2018. The unreasonable effectiveness of deep features as a perceptual metric, in: Proceedings of the IEEE conference on computer vision and pattern recognition, pp. 586–595.
- Zhou, S., Chan, K., Li, C., Loy, C.C., 2022. Towards robust blind face restoration with codebook lookup transformer. Advances in Neural Information Processing Systems 35, 30599–30611.

Supplementary Material

Visual comparisons. We have included additional visual comparison examples of generated super-resolution images using both GAN-based methods and our diffusion-based method, as shown in Figures 13, 14, and 15. Our diffusion-based approach generates super-resolution images with sharper details and more stable color staining that closely resemble high-resolution images. Furthermore, our method maintains texture information similar to the high-resolution ground truth images. Please zoom in to see the details more clearly.

Dataset distribution. We have provide the image names and their corresponding WSI ids in google drive. Please visit WSI IDs. for more information. There is no overlapping between training set and test set.

Analysis of Histo-Diffusion. We also explore how different types of degradation impact the Histo-Diffusion model, which consists of a stage 1 SwinIR restoration module and a stage 2 controllable diffusion module. Both stages maintain the same settings, with the primary difference being the type of degradation applied in stage 1. Here, HR images are intentionally degraded to simulate real-world histopathological conditions, resulting in degraded LR images. These LR images are then restored using the SwinIR module to produce I_{RM} .

For the degradation process, we utilize the degradation type from CodeFormer Zhou et al. (2022), known for its ability to enhance detail in specific face restoration tasks where detail retention is critical. Additionally, we compare with degradation type from Real-ESRGAN Wang et al. (2021) here, which involves a second-order degradation and offers broader applicability across various image super-resolution tasks. Both degradation types effectively handle real-world noise, blur, and compression artifacts in natural images, and we analyze their effectiveness on digital pathology images.

Moreover, we assess how training iterations influence the performance of the generated super-resolution images. Considering that prolonged training durations and high computational demands are significant challenges of diffusion models, we monitor performance across various training iterations. Additionally, to determine if extended training could lead to overfitting—a frequent issue with GANs—we evaluate the model’s performance at various training milestones (60k, 100k, 160k, and 205k iterations) across different datasets: PRAD-100, LUAD-100, and GBM-100. This evaluation allows us to observe changes in performance and assess the potential for overfitting as training progresses.

The results presented in Table 6 illustrate our findings. We compared different training iterations and degradation types, revealing that even with the smallest training iteration of 60k, the performance remains competitive. When comparing GAN-based and diffusion-based methods, even the least-performing model in Table 6 and Table 2 consistently surpasses GANs in ST-LPIPS, MUSIQ, NIQE, BRISQUE, and NRQM across all three datasets. Additionally, it shows superior LPIPS results for

LUAD-100 and GBM-100, indicating that the method generalizes well to different cancer types while maintaining high perceptual similarity. These results demonstrate that our approach can produce high quality super-resolution images that closely resemble high-resolution ground truths.

In comparing different degradation types, CodeFormer degradation performs better in full-reference IQA (LPIPS and ST-LPIPS), while Real-ESRGAN degradation excels in no-reference IQA (CLIP-IQA, MUSIQ, NIQE, BRISQUE, and NRQM). Both show competitive results compared to GANs, prompting the question of whether degradation simulation, crucial in GAN-based methods for mimicking real-world degradation Wang et al. (2021), is as important in diffusion-based super-resolution models.

In the forward phase, a diffusion model progressively adds noise to an image, simulating various real-world degradations. The reverse phase systematically removes the noise, restoring image details and reversing the degradation. This inherent mechanism addresses the degradation mimic problem in histopathology by methodically eliminating various forms of noise and artifacts.

In histopathology, degradation often arises from poor staining, variations in slide preparation, or suboptimal imaging conditions, leading to blurring, noise, and artifacts that obscure critical diagnostic information. Traditional methods struggle to replicate and correct these degradation patterns without matching training data. However, Histo-Diffusion provides a way to inherently address the degradation mimic problem in histopathology by learning to simulate and systematically eliminate noise and artifacts. This makes our diffusion-based super-resolution model highly suitable for enhancing image quality in fields like histopathology, where managing diverse and unpredictable degradations is crucial.

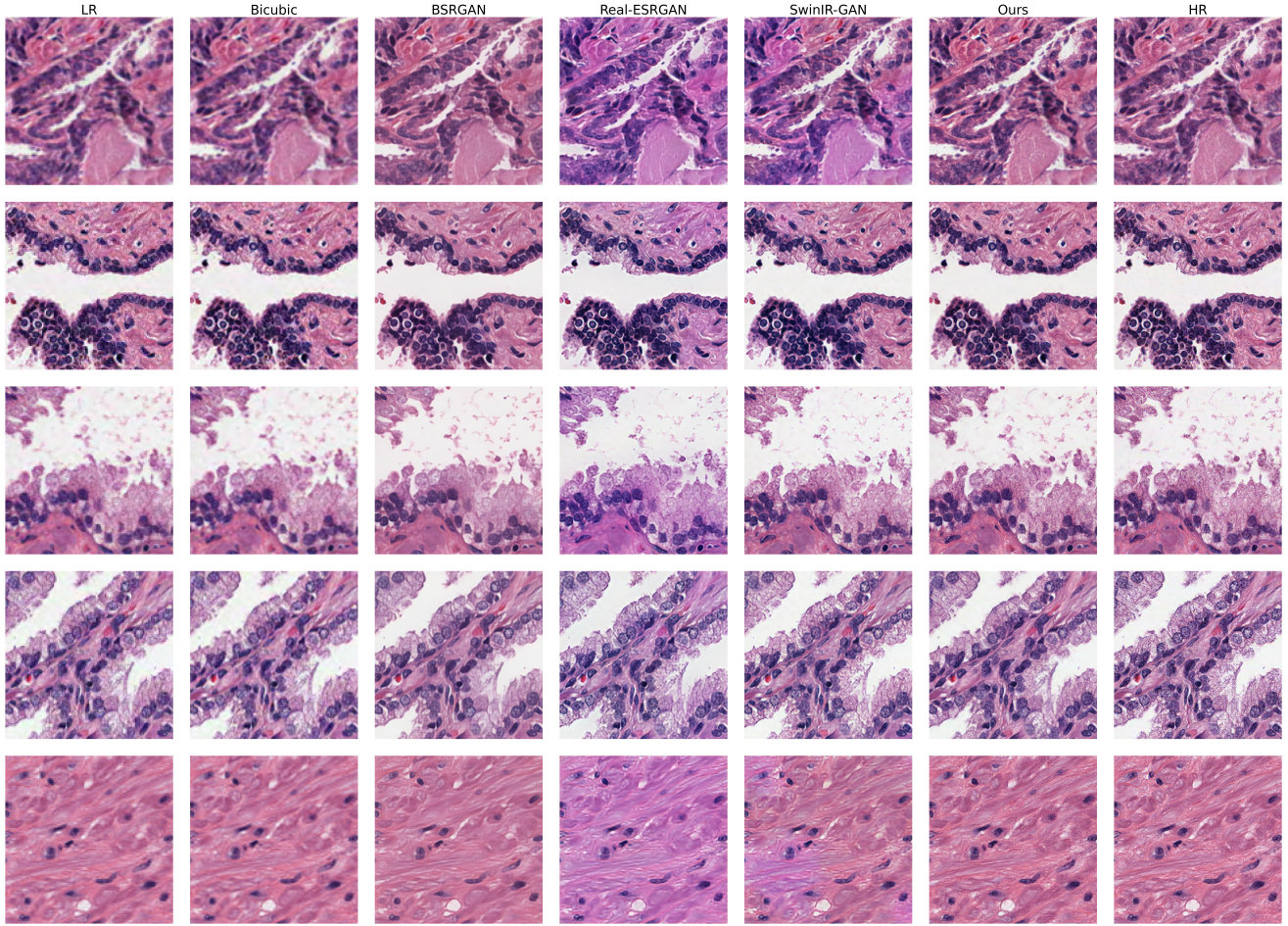


Fig. 13: Visual comparisons on PRAD-100 samples. Please zoom in for more details.

Table 6: Comparisons of different image degradations (Real-ESRGAN degradation vs CodeFormer degradation) for different iterations on histopathology image datasets with a 4× upsampling scale using our Histo-Diffusion. The best and worst results are highlighted in **bold** and *textit*.

Datasets	Iterations	Degradation	Metrics								
			PSNR↑	SSIM↑	LPIPS↓	ST-LPIPS↓	CLIP-IQA↑	MUSIQ↑	NIQE↓	BRISQUE↓	NRQM↑
PRAD-100	60k	Real-ESRGAN	24.67	0.5791	0.2415	<i>0.2160</i>	0.4769	47.51	4.92	25.39	6.66
		Codeformer	24.72	0.5880	0.2362	0.2097	0.4454	44.57	4.88	29.65	6.46
	100k	Real-ESRGAN	<i>24.44</i>	<i>0.5629</i>	<i>0.2453</i>	0.2138	0.4828	48.61	4.69	25.90	6.95
		Codeformer	24.89	0.6014	0.2280	0.2022	<i>0.4365</i>	43.82	4.99	29.70	6.25
	160k	Real-ESRGAN	24.84	0.5797	0.2358	0.2156	0.4731	47.31	4.71	26.60	6.87
		Codeformer	25.03	0.6081	0.2287	0.2089	0.4439	<i>43.49</i>	<i>5.08</i>	30.93	<i>6.16</i>
	205k	Real-ESRGAN	24.68	0.5741	0.2381	0.2126	0.4732	48.48	4.70	26.86	6.90
		Codeformer	24.86	0.5947	0.2279	0.2079	0.4559	45.00	4.95	<i>31.39</i>	6.34
LUAD-100	60k	Real-ESRGAN	24.41	0.6085	<i>0.2972</i>	<i>0.2497</i>	<i>0.4042</i>	43.01	5.07	27.77	5.45
		Codeformer	25.79	0.6629	0.2674	0.2313	0.4134	<i>41.50</i>	5.24	<i>34.57</i>	4.96
	100k	Real-ESRGAN	23.90	<i>0.5866</i>	0.2968	0.2472	0.4291	44.52	4.93	26.06	5.78
		Codeformer	26.03	0.6785	0.2606	0.2249	0.4181	42.41	5.26	32.41	4.93
	160k	Real-ESRGAN	24.39	0.6013	0.2922	0.2368	0.4186	44.20	4.78	27.62	6.04
		Codeformer	26.48	0.6935	0.2576	0.2290	0.4133	41.61	5.33	33.08	<i>4.81</i>
	205k	Real-ESRGAN	24.08	0.5902	0.2901	0.2307	0.4202	45.77	4.95	28.08	6.09
		Codeformer	25.92	0.6666	0.2526	0.2250	0.4309	43.22	5.12	33.14	5.15
GBM-100	60k	Real-ESRGAN	22.68	0.4768	0.3035	0.3826	0.5027	51.58	5.26	25.48	6.17
		Codeformer	23.04	0.5087	0.2888	0.3675	0.4819	47.96	5.19	28.78	5.78
	100k	Real-ESRGAN	22.10	<i>0.4425</i>	<i>0.3059</i>	0.3784	0.5115	52.53	4.92	21.70	6.70
		Codeformer	23.34	0.5357	0.2881	0.3628	<i>0.4650</i>	<i>46.09</i>	<i>5.53</i>	<i>31.70</i>	<i>5.42</i>
	160k	Real-ESRGAN	22.55	0.4617	0.2921	0.3784	0.5095	51.47	4.53	20.84	6.93
		Codeformer	23.25	0.5217	0.2822	0.3642	0.4767	47.39	5.05	28.36	5.85
	205k	Real-ESRGAN	22.41	0.4576	0.2988	0.3762	0.5126	53.38	4.77	21.75	6.74
		Codeformer	22.88	0.4950	0.2894	0.3663	0.4862	49.13	4.94	27.52	5.96

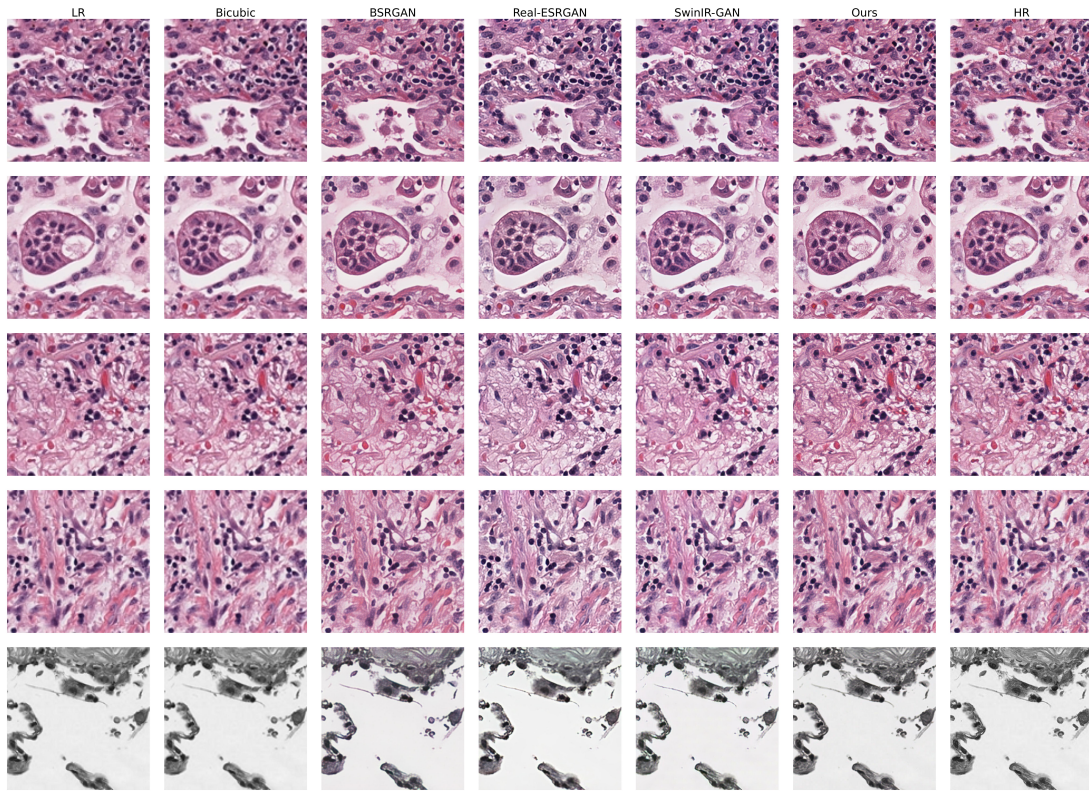


Fig. 14: Visual comparisons on LUAD-100 samples. Please zoom in for more details.

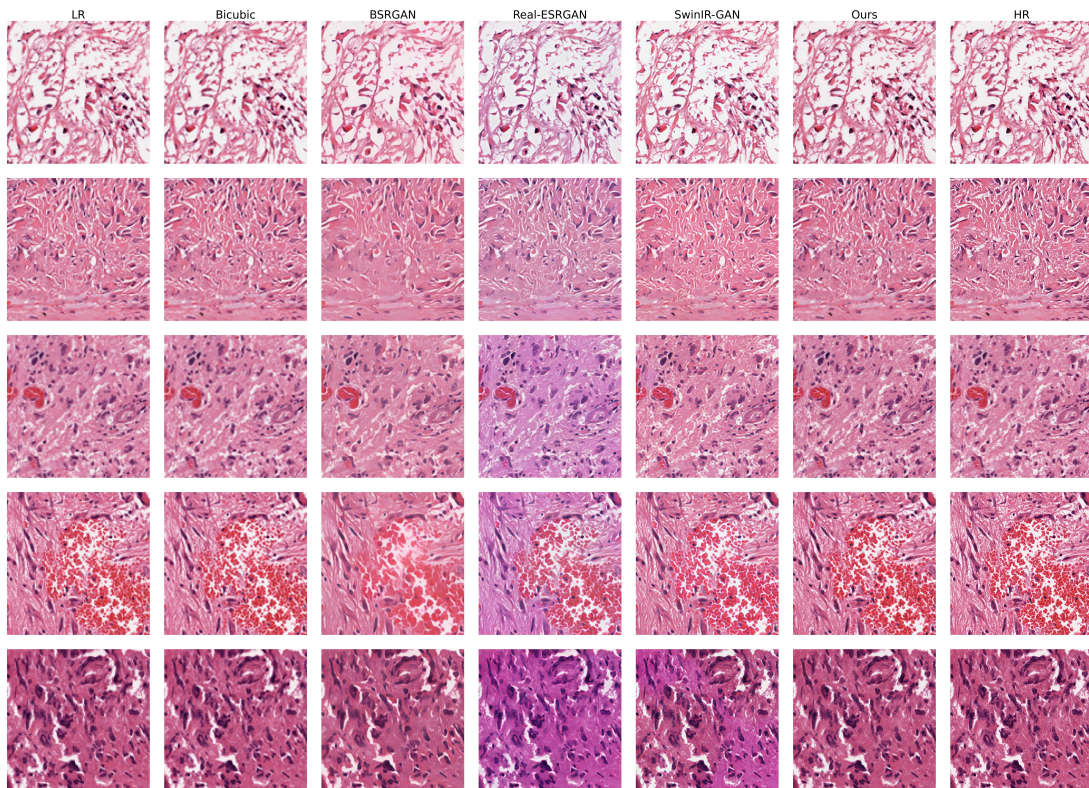


Fig. 15: Visual comparisons on GBM-100 samples. Please zoom in for more details.